Energy & Environmental Science

ROYAL SOCIETY OF CHEMISTRY

PAPER

View Article Online
View Journal | View Issue

Published on 30 September 2022. Downloaded by Yonsei University on 11/10/2022 12:23:28 AM.

Check for updates

Cite this: *Energy Environ. Sci.*, 2022, **15**, 4725

High-performance Sb_2S_3 photoanode enabling iodide oxidation reaction for unbiased photoelectrochemical solar fuel production†

Young Sun Park, Xiaoyan Jin, Jeiwan Tan, Hyungsoo Lee, Juwon Yun, Sunihl Ma, Gyumin Jang, Taehoon Kim, Sang Gi Shim, Kyungmin Kim, Jeongyoub Lee, Chan Uk Lee, Seong-Ju Hwang * and Jooho Moon *

Received 19th September 2021,
Accepted 26th September 2022

DOI: 10.1039/d1ee02940a

rsc.li/ees

The traditional photoelectrochemical (PEC) tandem configuration of hydrogen evolution reaction and oxygen evolution reaction (OER) demands a considerable potential of 1.8 V due to theoretical water splitting potential as well as a large overpotential mainly derived by sluggish OER kinetics. The iodide oxidation reaction (IOR) is a promising alternative to OER due to its low thermodynamic energy and two-electron-involved fast reaction kinetics. Herein, we report a high-performance catalyst-modified Sb_2S_3 photoanode to drive IOR. A compact thin-film-type Sb_2S_3 absorber is fabricated *via* solution processing based on a thorough understanding of the molecular interaction in the precursor ink state. Moreover, the deposition of a multilayered catalyst RuO_2 nanosheet and polydiallyldimethylammonium chloride not only efficiently enhances the charge transfer kinetics but also passivates the surface defects of the Sb_2S_3 absorber. The resulting photoanode exhibits an efficient photocurrent density of 10 mA cm^{-2} at 0.54 V compared to the normalized hydrogen electrode in hydroiodic acid. In conclusion, we demonstrate a bias-free PEC tandem device based on a RuO_2-modified Sb_2S_3 photoanode paired with a silicon photocathode, yielding an operation current density of 4 mA cm^{-2}.

Broader context

The photoelectrochemical (PEC) tandem device is a promising pathway to produce clean hydrogen fuel from abundant sunlight. However, hydrogen generation using traditional PEC tandem configuration suffers from significant thermodynamic energy for splitting water and kinetic barriers of oxygen evolution reaction. Therefore, it is highly demanding to explore alternative oxidation reactions (AORs) that not only require a low thermodynamic energy when coupled with the hydrogen evolution reaction but also reveal fast electrochemical reaction kinetics. Iodide oxidation reaction (IOR) is a prominent candidate for AOR, since IOR satisfies all these requirements. Here, we demonstrate high-performance RuO_2-modified Sb_2S_3 photoanode enabling IOR for unassisted solar-to-hydrogen conversion. The tandem configuration comprising the Sb_2S_3-based photoanode and silicon photocathode afforded an operation current density 4 mA cm^{-2}. The realization of high-efficiency tandem device demonstrates prospect potential of catalyst-modified Sb_2S_3 photoanode when combined with IOR as an AOR.

Introduction

A photoelectrochemical (PEC) tandem configuration comprising a photoanode (n-type semiconductor) and photocathode (p-type semiconductor) is a promising route for solar-to-hydrogen conversion without an external bias.[1] Conventional PEC tandem systems drive the hydrogen evolution reaction (HER) at the photocathode and the oxygen evolution reaction (OER) at the photoanode.[2,3] However, a considerable potential of 1.8 V is required to provide the thermodynamic driving force for splitting the water along with an overpotential to overcome the kinetic barriers at the electrode/electrolyte interfaces.[4,5] Particularly, OER necessitates a significant overpotential because of its sluggish kinetics involving a four-electron-transfer reaction, which hinders the overall PEC tandem performance.[6] Therefore, alternative oxidation reactions (AORs) have been explored that not only require a low thermodynamic driving energy but also exhibit rapid electrochemical reaction kinetics.

Among the various AORs for replacing OER, the iodide oxidation reaction (IOR) has emerged as a prominent candidate, since IOR requires a low thermodynamic energy of 0.54 V

Department of Materials Science and Engineering, Yonsei University, Seoul, 03722, Republic of Korea. E-mail: hwangsju@yonsei.ac.kr, jmoon@yonsei.ac.kr

† Electronic supplementary information (ESI) available. See DOI: https://doi.org/10.1039/d1ee02940a

Published on 30 September 2022. Downloaded by Yonsei University on 11/10/2022 12:23:28 AM.

when coupled with the HER.[7] Moreover, IOR exhibits fast reaction kinetics owing to its two-electron-transfer-involved oxidization of iodide to triiodide in strong acidic conditions, and the resulting species is considered as a value-added product because of its versatile utilization in the hygiene industry.[8] Indeed, iodide was photoelectrochemically oxidized by silicon microwire array photoanodes in a previous study.[9,10] Recently, Yao *et al.* developed a hybrid photoanode based on the bulk heterojunction between a covalent polymer network and mesoporous SnO_2 layer for IOR.[7] However, the photoanode exhibited a low photocurrent density of 3.3 mA cm^{-2} at 0.54 V compared to the normalized hydrogen electrode (V_{NHE}) with a positive onset potential of 0.43 V_{NHE} since the low crystallinity and short charge carrier diffusion length of the polymer cause charge carrier recombination within the bulk electrode. Moreover, the mesoporous absorber inevitably induces a direct contact between an electrolyte (or catalyst) and a conductive substrate, which acts as a shunting path and causing charge recombination.[11,12] Therefore, a high-performance low-cost photoanode that exhibits high crystallinity and long charge carrier diffusion while maintaining a compact morphology to prevent shunting is highly desirable for efficient IOR.

Recently, antimony trisulfide (Sb_2S_3), comprising earth abundant elements, has been proposed as a potential candidate for PEC devices.[13] The thermodynamically stable orthorhombic phase of Sb_2S_3 allows the easy formation of a highly crystalline absorber without a secondary phase, and Sb_2S_3 is an n-type semiconducting material that is suitable for photoanodes owing its long hole diffusion length ($\sim$180 nm) and high absorption coefficient ($>10^5$ cm^{-1}).[14,15] Particularly, Sb_2S_3 retains the ideal band gap energy of 1.6–1.8 eV for the front electrode in a solar fuel tandem device wherein the bottom electrode has an ideal band gap of 1.0–1.2 eV.[14,16] Moreover, the current dye-sensitized solar cell based on Sb_2S_3 has demonstrated sufficient iodide oxidation capabilities in an iodide/triiodide redox electrolyte, suggesting that it is a promising photoanode material for the PEC oxidation of iodide as an AOR for yielding hydrogen.[17] However, despite these superior optoelectrical properties, no study has reported the use of a Sb_2S_3-derived photoanodes for a bias-free tandem device that can drive HER coupled with IOR.

Herein, we prepared a thiourea–antimony ion complex containing a precursor solution for yielding the Sb_2S_3 absorber. The relationship between the thiourea–antimony stoichiometry and nucleation mechanism was elucidated *via* liquid Raman spectroscopy, from which a compact Sb_2S_3 absorber was fabricated. To enhance the catalytic activity, we implemented a layer-by-layer deposition of the RuO_2 nanosheet (RuO_2 NS) and polydiallyldimethylammonium chloride (PDDA) as a multilayered catalyst (denoted as RuO_2/PDDA) on top of the Sb_2S_3 absorber. The RuO_2/PDDA not only boosts the hole transfer kinetics but also passivates the surface defects of Sb_2S_3 absorber. Thus, the multilayered catalyst deposited on the Sb_2S_3 absorber (denoted as RuO_2/PDDA@SB photoanode) exhibits an IOR photocurrent density of 10 mA cm^{-2} at 0.54 V_{NHE} with a small onset potential of 0 V_{NHE} in a hydroiodic acid electrolyte (0.5 M H_2SO_4 + 0.1 M KI). We successfully demonstrated an unassisted solar-to-hydrogen conversion for a two-electrode tandem device comprising the RuO_2/PDDA@SB photoanode as the front electrode and the silicon photocathode as the bottom electrode. The tandem device was operated in a hydroiodic acid electrolyte without an external potential, delivering a photocurrent density of 4 mA cm^{-2}. This study demonstrates an unassisted PEC tandem device with a RuO_2-modified Sb_2S_3 photoanode and a Si photocathode that delivers a high efficient photocurrent density.

Results and discussion

A compact thin-film-type Sb_2S_3 absorber was fabricated using thiourea–$SbCl_3$ (TU–$SbCl_3$) precursor ink according to the in-depth understanding of the TU–$SbCl_3$ complex formation in solution. While the influence of the TU/$SbCl_3$ precursor ratio on the Sb_2S_3 film morphology has been previously reported, the surface coverage effect has been only considered with respect to the solar cell performance, without a thorough analysis of the precursor solution.[18] We prepared three different precursor inks by dissolving TU and $SbCl_3$ powders into 2-methoxyethanol (2ME) at different molar ratios of TU/$SbCl_3$ = 0.5, 1, and 2, which are referred to as 0.5TU–Sb, 1TU–Sb, and 2TU–Sb inks, respectively. To analyze the influence of the TU/$SbCl_3$ precursor stoichiometric ratio on the molecular interaction, each ink was characterized *via* liquid Raman spectroscopy (Fig. 1(a)). The molecular structure of TU–$SbCl_3$ was identified through the vibration modes of the precursor species. When $SbCl_3$ is dissolved in 2ME, the Sb–Cl bond diminishes and the Sb^{3+} ion is surrounded by solvent molecules. Correspondingly, the peak observed at $\sim$305 cm^{-1} (Sb^{3+} in 2ME) in Fig. 1(a) is assigned to the bonding vibration between Sb^{3+} ion and 2ME solvent molecule.[19] Interestingly, in the 0.5TU–Sb ink, the dominant peak of Sb^{3+} in 2ME was monitored, whereas it was diminished in both 1TU–Sb and 2TU–Sb inks. This implies that excess TU in the precursor ink markedly interacts with Sb^{3+} ions due to the strong complexation between Sb^{3+} ion and sulfur in TU molecule, as shown by the appearance of the Sb–S vibration peaks at 224–258 cm^{-1}.[20] The 0.5TU–Sb ink displayed a high-frequency Sb–S vibration peak at 258 cm^{-1} with higher intensity than the 1TU–Sb and 2TU–Sb inks. This denotes that the bonding strength of Sb–S in the 0.5TU–Sb ink is higher than that in the 1TU–Sb and 2TU–Sb inks. Furthermore, the formation of Sb–S bond in each ink clearly influences the C═S bond in TU, as expressed by the red shift of the C–S vibration peak (720–730 cm^{-1}) with respect to the C═S vibration peak (738 cm^{-1}). Contrastingly, the C–S vibration peaks were blue shifted in the order of 0.5TU–Sb < 1TU–Sb < 2TU–Sb, implying that the C–S bond weakens with increasing Sb–S bonding strength.

Based on the liquid Raman analysis, we schematically illustrate the molecular interaction in TU–$SbCl_3$ precursor inks in Fig. 1(b). When TU and $SbCl_3$ are dissolved in 2ME, the lone pair electrons of nitrogen in TU are delocalized, causing the electron configuration rearrangement of sulfur having a high electron density through which a strong bond can form

 This journal is © The Royal Society of Chemistry 2022

Published on 30 September 2022. Downloaded by Yonsei University on 11/10/2022 12:23:28 AM.

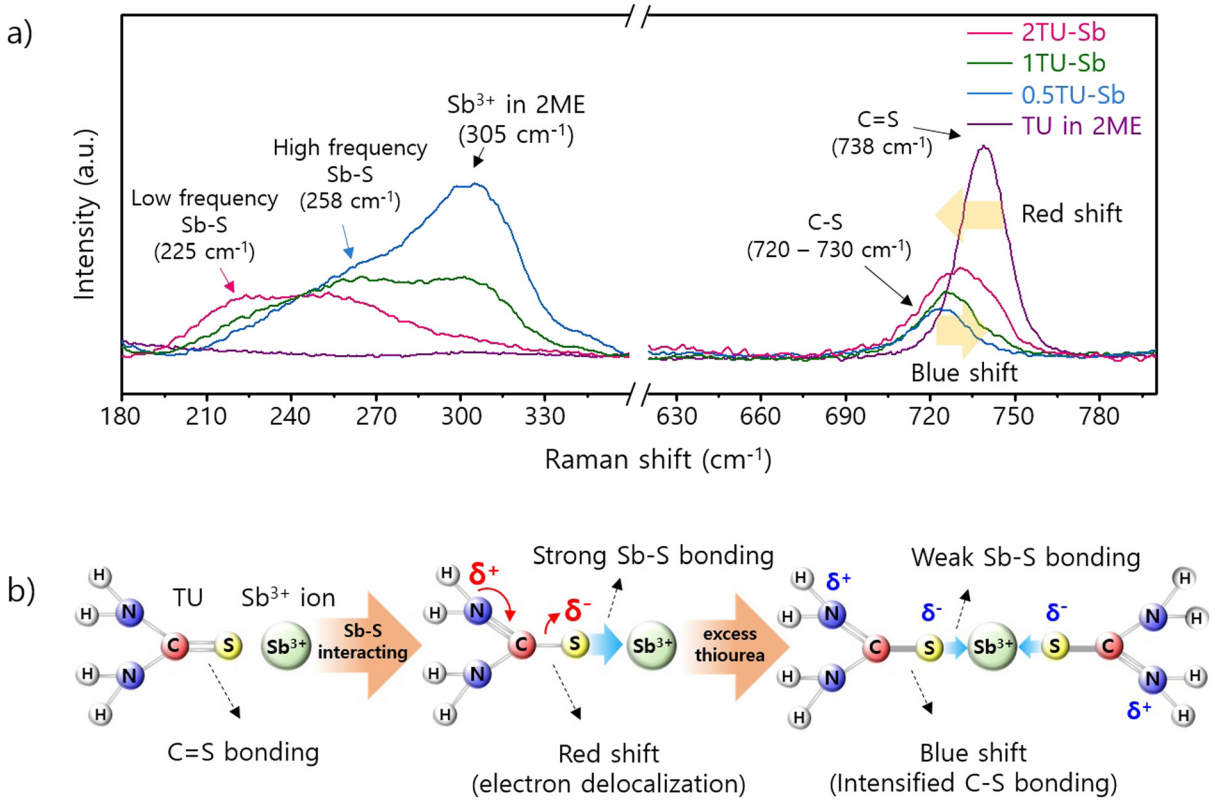

Fig. 1 Molecular structure analysis of three different precursor inks using liquid Raman spectroscopy (a) liquid Raman spectra for three different precursor inks and TU in 2ME. (b) Schematic of the molecular interaction between TU and Sb^{3+} ion in 2ME and weakening Sb–S bonding (*i.e.*, intensified C–S bonding) upon the addition of excess TU.

between sulfur and Sb^{3+} ion.[21] As the Sb–S bond formed, the electron delocalization diminished the double bonding property of the carbon–sulfur interaction, as demonstrated by the red shift of the C–S bonding vibration peak of the 0.5TU–Sb, 1TU–Sb, and 2TU–Sb inks compared to the C═S bonding vibration peak of TU in 2ME ink. When excess TU was present in the precursor ink, Sb^{3+} ions were surrounded by considerable TU. Accordingly, the electron density distributed around the sulfur in TU decreased to satisfy the charge neutrality. Consequently, the Sb–S bonding weakened because of the low electron density involved in the Sb–S bonding, whereas the C–S bonding peak blue shifted due to the intensified C–S bonding (*i.e.*, weakening Sb–S boning). Therefore, the 0.5TU–Sb ink exhibits strong Sb–S bonding (*i.e.*, weak C–S boning), whereas 1TU–Sb and 2TU–Sb inks exhibit weak Sb–S bonding (*i.e.*, strong C–S bonding), because excess TU is present in the precursor inks, which weakens the Sb–S bonding (*i.e.*, intensified C–S bonding).

To analyze the influence of the molecular interaction between Sb and S on the resulting Sb_2S_3 film morphology, three different molecular inks were spin-coated onto the TiO_2/doped tin oxide (FTO)/glass substrate. The TiO_2 deposited on the FTO substrate functions as an electron transport layer in the photoanode because TiO_2 with the positive valence band can block hole extraction to the back contact which leads to charge carrier recombination (as shown in Fig. S1, ESI†). The Sb_2S_3 absorber morphologies varied depending on the precursor stoichiometry, as examined by scanning electron microscopy (SEM; Fig. 2(a)). Interestingly, the 0.5TU–Sb-ink-derived absorber exhibited closely packed cuboid morphology with sharp facets, while the absorber based on the 1TU–Sb and 2TU–Sb inks comprised enlarged grains and occasional pinholes, indicating that the grain size and pinhole density in the absorber layer increase with the increasing TU/$SbCl_3$ ratio in the molecular ink (*i.e.*, decreasing Sb–S bonding strength). The possible formation mechanism of the Sb_2S_3 absorbers depending on the precursor stoichiometry is schematically shown in Fig. 2(b). In the 0.5TU–Sb ink, Sb ions interact with relatively less number of TU molecules, thus affording strong Sb–S bonding (*i.e.*, weak C–S bonding). In contrast, in the 1TU–Sb and 2TU–Sb inks, the Sb ions interact with the considerable TU molecules that sufficiently surround them, affording weak Sb–S bonding (*i.e.*, strong C–S bonding). When the 0.5TU–Sb ink was utilized, fine particles of Sb_2S_3 were uniformly distributed on the substrate (Fig. S2a–c, ESI†). While, when the 1TU–Sb and 2TU–Sb inks were utilized, a few large particles of Sb_2S_3 were nucleated without complete surface coverage. In the 0.5TU–Sb ink, we speculate that the strong Sb–S bonding easily breaks the C–S bond in TU and boosts the nucleation rate during the solvent drying/annealing process, and thus, a large number of nuclei can be generated throughout the substrate, consequently yielding a closely packed small cuboid-like Sb_2S_3 film with

Published on 30 September 2022. Downloaded by Yonsei University on 11/10/2022 12:23:28 AM.

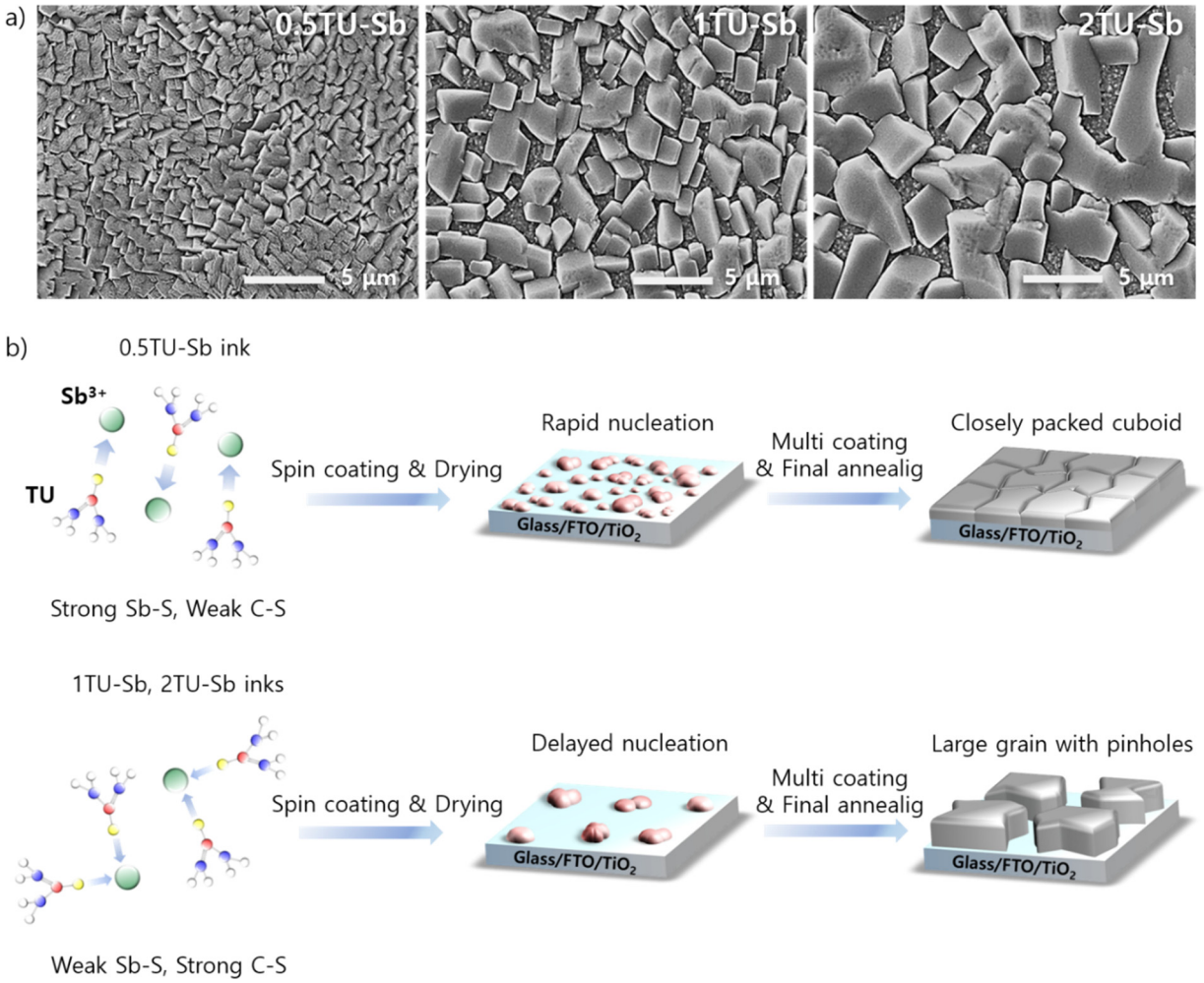

Fig. 2 (a) Top-view SEM images of Sb_2S_3 absorbers obtained from three different precursor inks. (b) Schematic of the nucleation mechanism for Sb_2S_3 films derived using three different precursor inks. The 0.5TU–Sb ink exhibits strong Sb–S molecular interaction, facilitating the nucleation event during the annealing and eventually affording a closely packed small-cuboid-like film. In contrast, both 1TU–Sb and 2TU–Sb inks exhibit weak Sb–S molecular interaction, delaying the nucleation and yielding a large grained film with occasional pinholes.

sharp facets.[22] Contrastingly, in the 1TU–Sb and 2TU–Sb inks, less nucleation of Sb_2S_3 occurs because the weak Sb–S bonding hardly cleaves the C–S bond, delaying the nucleation events and limiting the number of nuclei from which large-grained Sb_2S_3 films with high pinhole density are obtainable. Among the three different absorbers, only the 0.5TU–Sb ink forms a Sb_2S_3 absorber that is suitable for IOR owing to the pinhole free morphology.

The phase evolution of the 0.5TU–Sb-ink-based Sb_2S_3 absorber was analyzed *via* X-ray diffraction (XRD). As shown in Fig. S3a (ESI†), all the peaks well matched with the stibnite antimony trisulfide phase (JCPDF No. 006-0474).[23] Raman spectroscopy accurately determines the vibrational modes of phase-pure Sb_2S_3. The Raman spectrum depicted a strong peak of A_g mode (283 cm^{-1}, 305 cm^{-1}) and relatively small peaks of B_{3g} (237 cm^{-1}) and B_{1g} (188 cm^{-1}) modes (Fig. S3b, ESI†). The A_g and B_{3g} modes are attributed to the Sb–S vibration modes, whereas B_{1g} (188 cm^{-1}) stems from the S–Sb–S antisymmetric vibration mode.[24] These observations indicate that the solution-processed Sb_2S_3 absorber retains high crystallinity and phase purity without a secondary phase or impurities. The atomic composition of Sb_2S_3 was determined *via* energy-dispersive X-ray spectroscopy (EDX). The 0.5TU–Sb-ink-derived Sb_2S_3 absorber maintained an accurate stoichiometry of S/Sb ∼ 1.5 (Table S1, ESI†) because excess $SbCl_3$ with a low boiling point of 220.3 °C tends to be volatile during annealing at 350 °C.[25] Moreover, the statistics of S/Sb ratio obtained from ten samples of 0.5TU–Sb-ink-based Sb_2S_3 absorbers indicated that the average S/Sb ratio was nearly 1.49, demonstrating the reliability of EDX analysis (Fig. S4, ESI†) Furthermore, the band gap of the 0.5TU–Sb-ink-based Sb_2S_3 absorber was estimated using the Tauc plot of ultraviolet-visible (UV-Vis) absorption spectra (Fig. S5a and b, ESI†) based on eqn (1):

$$(\alpha h\nu)^n = A(h\nu - E_g) \quad (1)$$

where $h\nu$ is the energy of incident photons (eV), A is a numerical constant, E_g is the optical band gap of the material (eV), α is the absorption coefficient, and n is 2 for direct band gap materials

 This journal is © The Royal Society of Chemistry 2022

Published on 30 September 2022. Downloaded by Yonsei University on 11/10/2022 12:23:28 AM.

such as Sb_2S_3.[26] The band gap of the 0.5TU–Sb-ink-based Sb_2S_3 absorber calculated by the Tauc plot was 1.64 eV, which is close to that reported in literature (1.6–1.8 eV).

To enhance the catalytic activity, we implemented a layer-by-layer deposition of RuO_2/PDDA onto the 0.5TU–Sb-ink-based Sb_2S_3 absorber (see Experimental section for details). As shown in Fig. S6a and b (ESI†), linear sweep voltammetry (LSV) and chronoamperometric measurements of the RuO_2/PDDA deposited on the FTO (denoted as RuO_2/PDDA/FTO) were carried out by standard three-electrode configuration in 300 mL of a hydroiodic acid electrolyte (0.5 M H_2SO_4 + 0.1 M KI), implying not only superior IOR catalytic activity but also durable stability over 10 h. According to theoretical calculation, 0.1 M of iodide ions in 300 mL will be exhausted after long-term operation more than 100 h under the current density of 10 mA cm^{-2} and electrode active area of 0.5 cm^2. Moreover, it should be noted here that the chronoamperometry test was conducted without membrane separating working electrode and counter electrode, inducing triiodide generated at working electrode to be partially reduced back to iodide at counter electrode.[7] Therefore, the concentration of iodide barely influenced on the current density of RuO_2/PDDA/FTO during the IOR stability test. The cross-sectional microstructure of the RuO_2/PDDA@SB photoanode was analyzed *via* transmission electron microscopy (TEM). The low-magnification TEM image shows that the Sb_2S_3 absorber surface is covered with 50 nm-thick RuO_2/PDDA (Fig. 3(a)). Fig. 3(b) and (c) illustrates

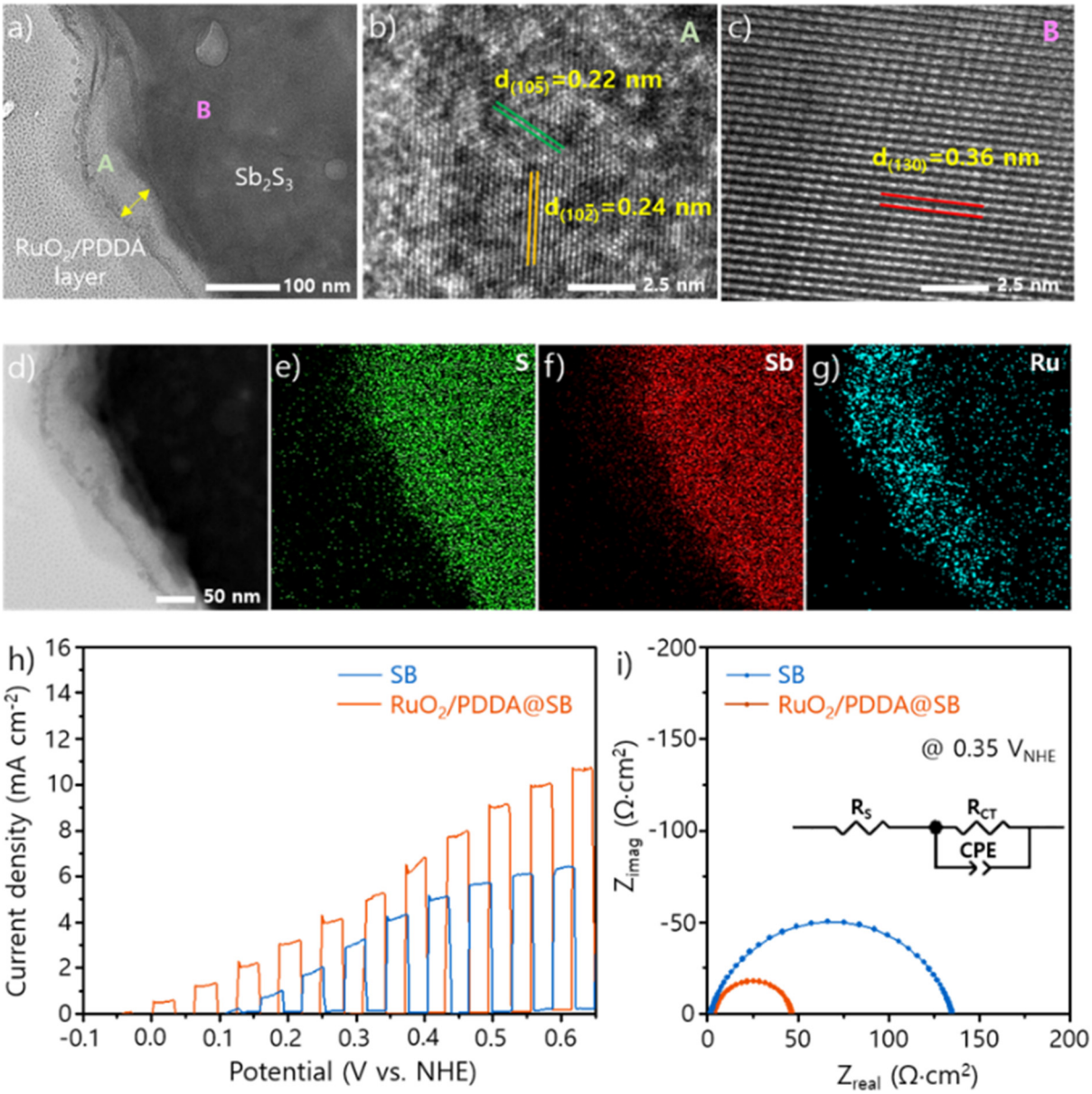

Fig. 3 (a) TEM image of the RuO_2/PDDA@SB photoanode. (b) HR-TEM image of the marked area of A. (c) HR-TEM image of the marked area of B. (d) STEM image of the RuO_2/PDDA@SB photoanode. EDX mapping of (e) Sb, (f) S, and (g) Ru. (h) LSV curves and (i) Nyquist plots of EIS spectra for both SB and RuO_2/PDDA@SB photoanodes in hydroiodic acid electrolyte (~pH 1).

Published on 30 September 2022. Downloaded by Yonsei University on 11/10/2022 12:23:28 AM.

the high-resolution TEM images revealing the surface and inner parts of the RuO_2/PDDA@SB photoanode, marked as A and B in Fig. 3(a), respectively. The lattice structure of RuO_2 NS is well displayed in Fig. 3(b), and the lattice fringes with distances of 0.22 and 0.24 nm clearly represent the crystalline RuO_2 NS, which is in good agreement with the interplanar spacing of the $(10\bar{5})$ and $(10\bar{2})$ planes, respectively.[27] Moreover, the lattice spacing of 0.36 nm corresponds to the (130) plane of Sb_2S_3, indicating the high crystallinity of the Sb_2S_3 absorber (Fig. 3(c)), which well matches with the XRD result.[28] To further clarify the elemental distribution of the RuO_2/PDDA@SB photoanode, scanning transmission electron microscopy (STEM) and EDX mapping were performed (Fig. 3(d)–(g)). This analysis indicates that the Ru element was uniformly distributed over the Sb_2S_3 absorber surface, confirming the RuO_2/PDDA are well deposited onto Sb_2S_3. Furthermore, as seen in Table S2 (ESI†), the atomic ratio of S/Sb determined by TEM-EDX analysis was nearly 1.49, which well matched with SEM-EDX analysis (Fig. S4, ESI†).

The PEC iodide oxidation performance of the 0.5TU–Sb-ink-derived Sb_2S_3 absorber without RuO_2/PDDA (denoted as the SB photoanode) and the RuO_2/PDDA@SB photoanode was characterized by a three-electrode configuration in a hydroiodic acid electrolyte. Fig. 3(h) shows LSV curves of the SB and RuO_2/PDDA@SB photoanodes. The photocurrent density of the SB photoanode was approximately 6 mA^{-2} at 0.54 V_{NHE} with an onset potential of 0.12 V_{NHE}. In contrast, the RuO_2/PDDA@SB photoanode not only displayed a negative onset potential (0 V_{NHE}) as compared with SB photoanode but also generated an efficient photocurrent density of 10 mA cm^{-2} at 0.54 V_{NHE}, which is 67% higher than that of the SB photoanode. Furthermore, the RuO_2/PDDA-modified 1TU–Sb- and 2TU–Sb-ink-based Sb_2S_3 absorbers afforded a low photocurrent density with a significant dark current as the catalyst layers deposited on the substrate through the pinholes of absorber act as shunting paths (Fig. S7, ESI†). To elucidate the catalytic activity of the RuO_2/PDDA layer on IOR performance, incident photocurrent conversion efficiency (IPCE) measurements for both SB and RuO_2/PDDA@SB photoanodes were performed (Fig. S8, ESI†). The RuO_2/PDDA@SB photoanode yielded a maximum IPCE of 35% up to the absorption edge (775 nm), whereas SB photoanode exhibited a relatively lower IPCE of 20% at the same wavelength range. The current density calculated from the IPCE values matches with the LSV results. The improved PEC performance may be attributed to the better catalytic activity and/or surface passivation effect of the RuO_2/PDDA-multilayered catalyst as the electrocatalyst functions as an active site for enhancing the charge transfer kinetics and a passivation layer for alleviating the surface states of Sb_2S_3 absorber.[29]

Electrochemical impedance spectroscopy (EIS) was performed at 0.35 V_{NHE} to investigate the charge transfer processes during the PEC iodide oxidation (Fig. 3(i)). Nyquist plots were obtained under illumination conditions and then fitting was performed with a Randles–Ershler circuit model (inset of Fig. 3(i)), where R_S is the series resistance and R_{CT} and CPE represent the charge transfer resistance and constant phase element respectively, at the electrode/electrolyte interface. The arc radius of the RuO_2/PDDA@SB photoanode is smaller than that of the SB photoanode, and Table S3 (ESI†) summarizes the deconvoluted charge transfer resistances. The lower R_{CT} value for RuO_2/PDDA@SB photoanode than the SB photoanode indicates the enhanced charge carrier transfer kinetics from electrode to electrolyte due to the RuO_2/PDDA catalyst,[30] as demonstrated by the substantial RuO_2/PDDA catalytic activity (Fig. S6, ESI†). To further identify the surface charge carrier transfer kinetics, we performed intensity-modulated photovoltage spectroscopy (IMVS). Nyquist plots of the typical IMVS spectra for the two photoanodes are displayed in Fig. S9 (ESI†). The charge carrier time constant (τ_n) at which recombination occurs is calculated using $\tau_n = (1/2\pi f_{min})$, where f_{min} denotes the frequency of the lowest point in the IMVS spectra. The RuO_2/PDDA@SB photoanode displayed significantly longer charge carrier life time (680.04 ms) than the SB photoanode (8.73 ms). This implies that the RuO_2/PDDA catalyst enables the efficient transfer of the photoinduced holes to the electrolyte and suppresses the charge carrier recombination at the electrode/electrolyte interface.[31]

Kelvin probe force microscopy (KPFM) was performed to verify the surface passivation effect of the RuO_2/PDDA catalyst. KPFM can elucidate not only the topographic information of the Sb_2S_3 absorber but also the contact potential difference (V_{CPD}) depending on the presence of the RuO_2/PDDA catalyst. Atomic force microscopy (AFM) topography images of the two photoanodes exhibited almost identical roughness with root-mean-square values in the 45–50 nm range (Fig. S10a and d, ESI†). Furthermore, the RuO_2/PDDA@SB photoanode exhibited higher V_{CPD} values than the SB photoanode (Fig. S10b and e, ESI†). Generally, a defect-rich thin film possesses a comparatively low V_{CPD} value, and the V_{CPD} value increases when the surface defects are passivated.[32] Therefore, an enlarged V_{CPD} value can be attributed to the alleviated surface states of the Sb_2S_3 absorber *via* the deposition of the RuO_2/PDDA catalyst. Additionally, the CPD difference between the irradiation and dark conditions indicates the surface photovoltage (SPV). The SPV value for the RuO_2/PDDA@SB photoanode was 171 mV, which is larger than that for the SB photoanode (96 mV), demonstrating better charge separation capability without recombination (Fig. S10c and f, ESI†).[33] Moreover, Mott–Schottky (MS) measurement in the dark condition was performed at 10 kHz frequency (Fig. S11, ESI†). The two photoanodes exhibited a positive slope, denoting n-type semiconductors. Notably, the smaller slope of the RuO_2/PDDA@SB photoanode than that of the SB photoanode indicates a higher charge carrier density of 3.67×10^{17} cm^{-3}; that of the SB photoanode is 2.44×10^{16} cm^{-3}. This observation clearly verifies that RuO_2/PDDA reduces the charge carrier recombination by passivating the surface defect states of the Sb_2S_3 absorber. Moreover, the obtained flat band potential cathodically shifts after the RuO_2/PDDA deposition, which is in accordance with the onset potential negatively shifting during the LSV measurement under illumination.

The chemical bonding characteristics of Sb_2S_3 and RuO_2/PDDA and their interfacial interaction in the RuO_2/PDDA@SB

 This journal is © The Royal Society of Chemistry 2022

Published on 30 September 2022. Downloaded by Yonsei University on 11/10/2022 12:23:28 AM.

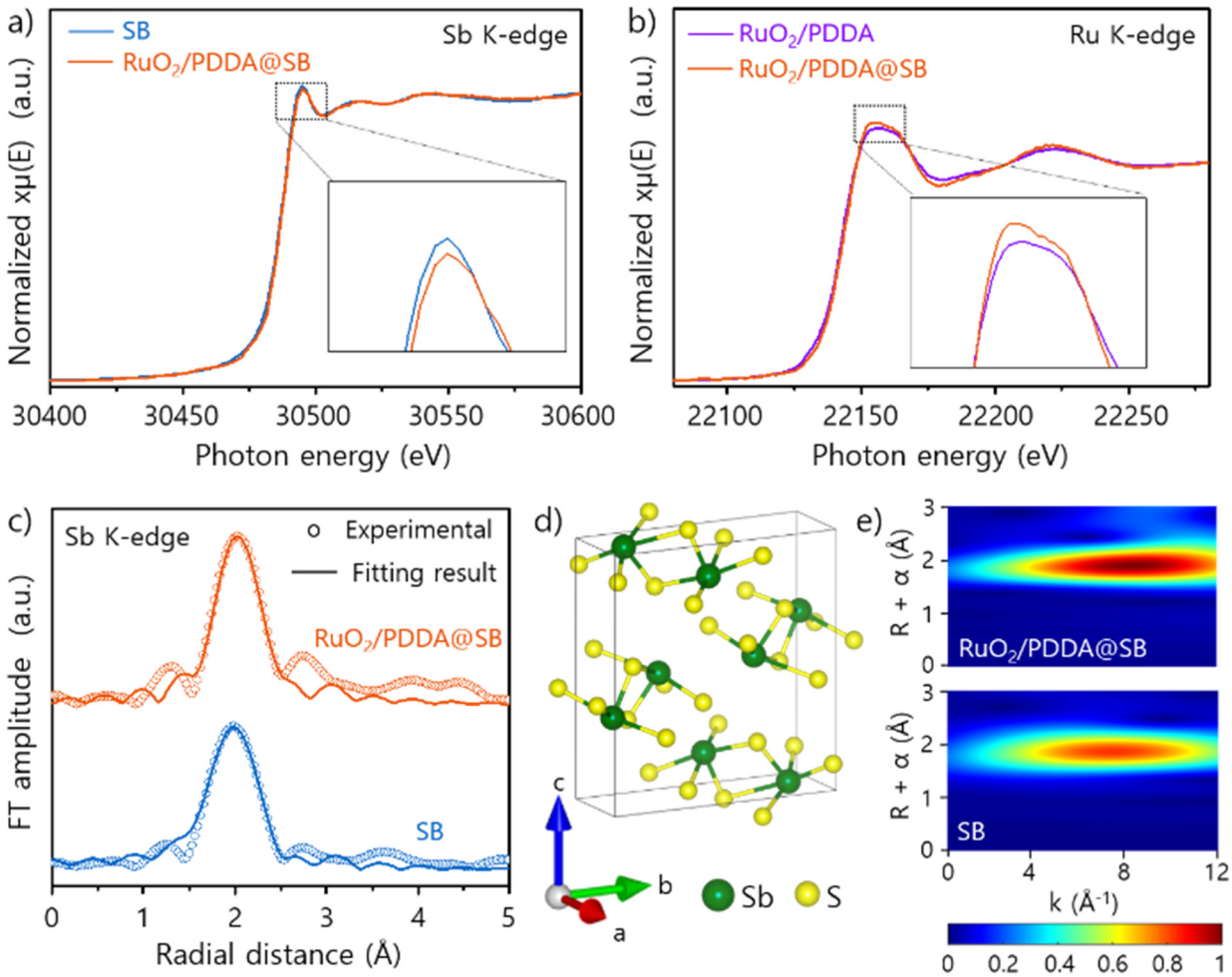

Fig. 4 (a) Sb K-edge XANES spectra, (b) Ru K-edge XANES spectra, and (c) Sb K-edge FT-EXAF spectra. (d) Crystal structure of Sb_2S_3. (e) Contour plot of the wavelet-transformed EXAFS data for the SB and RuO_2/PDDA@SB photoanodes.

photoanode were further analyzed using X-ray absorption spectroscopy (XAS) to elucidate the surface passivation effect. As presented in the Sb K-edge X-ray absorption near-edge structure (XANES) spectra of Fig. 4(a), both the photoanodes display nearly identical spectral features, including an intense resonance peak corresponding to the dipole-allowed 1s → 5p transition,[34] indicating the maintenance of the Sb_2S_3 phase after RuO_2/PDDA deposition. A closer inspection revealed that RuO_2/PDDA deposition slightly depressed the peak intensity. Since the intensity of the resonance peak is proportional to the density of the unoccupied final 5p orbital,[35] the observed peak depression can be interpreted as evidence of interfacial coordinative bonding between Sb^{3+} ions of Sb_2S_3 and the oxygen atoms of the RuO_2 NS layers and/or nitrogen ligands of intervened PDDA layers, which increases the Sb 5p electron density. As shown in Fig. 4(b), the RuO_2/PDDA@SB photoanode exhibited similar Ru K-edge XANES spectral features as RuO_2/PDDA, confirming the retention of the layered RuO_2 structure after the deposition on the SB photoanode. Similar to Sb K-edge region, an intense resonance peak related to the dipole-allowed 1s → 5p transition was discernible for both the materials.[36] The peak intensity was notably stronger for the RuO_2/PDDA@SB photoanode than that for RuO_2PDDA, indicating the electron density decrease in the Ru 5p state after the deposition on the SB photoanode. Since the interfacial chemical interaction of RuO_2 NS with Sb_2S_3 layer and/or intervened PDDA layer weakens the Ru–O bond in terms of bond competition,[37] the resulting depression of the Ru–O bond covalency decreased the electron density in the Ru 5p orbitals and consequently increased the resonance peak. Moreover, since the amount of RuO_2 is significantly less than that of Sb_2S_3 in the RuO_2/PDDA@SB photoanode, the spectral modification upon the deposition was found to be more prominent for the Ru K-edge region than for the Sb K-edge region.

The RuO_2/PDDA deposition effect on the local structure of the Sb_2S_3 layer was quantitatively examined with the Sb K-edge extended X-ray absorption fine structure (EXAFS) analysis. As depicted in Fig. 4(c), both the SB and RuO_2/PDDA@SB photoanodes exhibit quite similar Fourier transformed EXAFS (FT-EXAFS) spectra, including a strong FT peak at ∼2.1 Å corresponding to the Sb–S coordination shell. The EXAFS data of both the photoanodes could be well reproduced with the

Published on 30 September 2022. Downloaded by Yonsei University on 11/10/2022 12:23:28 AM.

Sb_2S_3 structure (Fig. 4(d)), verifying the maintenance of the Sb_2S_3 structure before and after RuO_2/PDDA deposition. As summarized in Table S4 (ESI†), the coordination number (CN) of the Sb–S bond was determined to be 4.0 for the SB photoanode, which is smaller than the crystallographic value of the Sb_2S_3 phase (CN = 5) (Fig. 4(d)),[38] indicating the presence of sulfur vacancy. Comparatively, the RuO_2/PDDA@SB photoanode exhibited a larger CN of 4.7, clearly demonstrating the passivation of the defective Sb_2S_3 layer *via* the formation of interfacial Sb–O/N bonds with RuO_2 and/or PDDA layers. Such an interfacial bond formation was further verified *via* Sb K-edge wavelet transform (WT) analysis, which shows the higher intensity of the Sb–S/O/N bond-related contour for RuO_2/PDDA@SB than that for SB (Fig. 4(e)). The Debye–Waller (σ^2) factor, which reflects the degree of structural disorder, decreased upon the deposition with RuO_2/PDDA, denoting the improvement of the surface structural order due to the surface passivation of Sb_2S_3.[39]

The surface chemical states and atomic interaction between the Sb_2S_3 absorber and RuO_2/PDDA catalyst were analyzed *via* X-ray photoelectron spectroscopy (XPS). As shown in Fig. S12a and b (ESI†), the Sb 3d and O 1s spectrum revealed two peaks at 538.8 and 529.5 eV, corresponding to Sb $3b_{3/2}$ and Sb $3b_{5/2}$, respectively, representing the Sb–S bond for Sb_2S_3.[40] Furthermore, for the SB photoanode, two peaks were located at 539.5 and 530.4 eV that are assignable to the Sb–O interaction,[41] indicating the existence of native Sb_2O_3 phase at the surface of Sb_2S_3 absorber, verifying the O–Sb peak located at 532.3 eV (Fig. S12a, ESI†).[42] The RuO_2/PDDA@SB photoanode exhibited a higher intensity for the Sb–O and O–Sb bonds than the SB photoanode. Moreover, the Sb–N bond peaks at 540.2 and 530.98 eV and the Ru–O–Ru bond peak at 528. 7 eV occurred after RuO_2/PDDA deposition (Fig. S12b, ESI†).[42,43] This indicates that the RuO_2/PDDA catalyst modification on the Sb_2S_3 surface increases the Sb–O bonds and generates the Sb–N bond, implying that oxygen atoms from RuO_2 NS and/or nitrogen ligands of intervened PDDA were inserted into the sulfur vacancy of Sb_2S_3, which is in agreement with the XAS results. The high-resolution S 2p spectra exhibited 162.7 and 161.5 eV peaks corresponding to S–Sb coordination,[40] and these two peaks significantly shifted toward lower binding energies after RuO_2/PDDA deposition (Fig. S12c, ESI†). This downward shift is attributed to the enhanced electron density around S^{2-}, suggesting that the Sb^{3+} ions weakly attract the electrons of S^{2-} with increasing CN of Sb^{3+} (*i.e.*, passivation of the sulfur vacancy).[44] The peaks at 163.4 and 164.8 eV of the RuO_2/PDDA@SB photoanode indicate the generation of the S–Ru bond because of the highly electronegative S^{2-} ion.[45,46] This S–Ru coordination may serve as an additional active site for halide oxidation.[47]

Herein, we demonstrated a bias-free PEC tandem device for solar-to-hydrogen conversion by combining the HER on a silicon-based photocathode with the iodide oxidation on a RuO_2/PDDA@SB photoanode. As schematically shown in Fig. 5(a), the solar light penetrates the front of the Sb_2S_3 photoanode and then passes through the electrolyte to the Si photocathode, enabling the overall reaction as expressed by following eqn (2).

$$2H^+ + 3I^- \rightarrow H_2 + I_3^- \quad (2)$$

The Si photocathode employed for the tandem device displayed efficient HER performance (−14 mA cm^{-2} at 0 V_{NHE} and an onset potential of 0.4 V_{NHE} in a hydroiodic acid electrolyte) as the bottom electrode (Fig. 5(b)). The operation point of the HER tandem device coupled with IOR, as determined by the crossing point of two LSV curves, was approximately 4.0 mA cm^{-2} at 0.25 V_{NHE}, indicating the possibility of solar-to-hydrogen conversion without an applied bias. To measure the actual tandem efficiency, the LSV curve of the Si‖RuO_2/PDDA@SB two-electrode tandem cell was obtained under simulated 1 sun light condition, exhibiting a photocurrent of 4.0 mA cm^{-2} at zero bias (Fig. 5(c)). This photocurrent density well matches with the predicted value according to the operation point of LSV curves (Fig. 5(b)), and this value is a high photocurrent density compared to other unbiased PEC tandem devices involving HER–OER or HER–AOR paired systems (Table S5, ESI†). To confirm the beneficial effect of IOR on the improved hydrogen generation efficiency, the OER activity of the RuO_2/PDDA@SB photoanode was measured in sulfuric acid (0.5 M H_2SO_4) without the iodide hole scavenger (Fig. S13a, ESI†). The LSV curve of the OER exhibited significantly lower photocurrent (2.5 mA cm^{-2} at 0.54 V_{NHE}) and positive shift of the onset potential (0.20 V) than that of the IOR. Considering the difference (0.69 V) between theoretical potentials of IOR and OER, this shift is smaller than theoretical value. The onset potential is determined by photovoltage as well as theoretical redox potential, assuming that the kinetic overpotentials of IOR and OER are identical.[48] The photovoltage at semiconductor-liquid junction develops by the difference between the Fermi level of semiconductor and redox potential of electrolyte.[49] Therefore, the photovoltage of RuO_2/PDDA@SB under IOR and that under OER were not identical due to different electrolyte condition, so that the onset was smaller than 0.69 V. Furthermore, light-on transient spikes at the more positive potential than 0.4 V_{NHE} were observable. Since the kinetics of hole transfer to electrolyte under OER condition is sluggish, the photon-induced holes are accumulated at the electrode/electrolyte interface. This hole accumulation induces severe oxidation reaction of Sb_2S_3 at the high anodic potential according to Pourbaix diagram,[50] resulting in partially oxidized surface states. These surface states likely play as a recombination center interfering the OER, thus the transient current spike behaviour is observed. By contrast, these spikes completely disappeared under IOR condition as rapid hole transfer kinetics of two-electron-transfer involved IOR prevented hole accumulation. The HER–OER tandem in a configuration of Si‖RuO_2/PDDA@SB afforded a photocurrent density of 1 mA cm^{-2} at zero bias, which is considerably less than that delivered by the HER–IOR tandem configuration (Fig. S13b, ESI†). The photocurrent density of 1 mA cm^{-2} yielded by Si‖RuO_2/PDDA@SB at zero bias was likely induced not by side reaction but by overall water splitting because the intersection point of the independently estimated

 This journal is © The Royal Society of Chemistry 2022

Published on 30 September 2022. Downloaded by Yonsei University on 11/10/2022 12:23:28 AM.

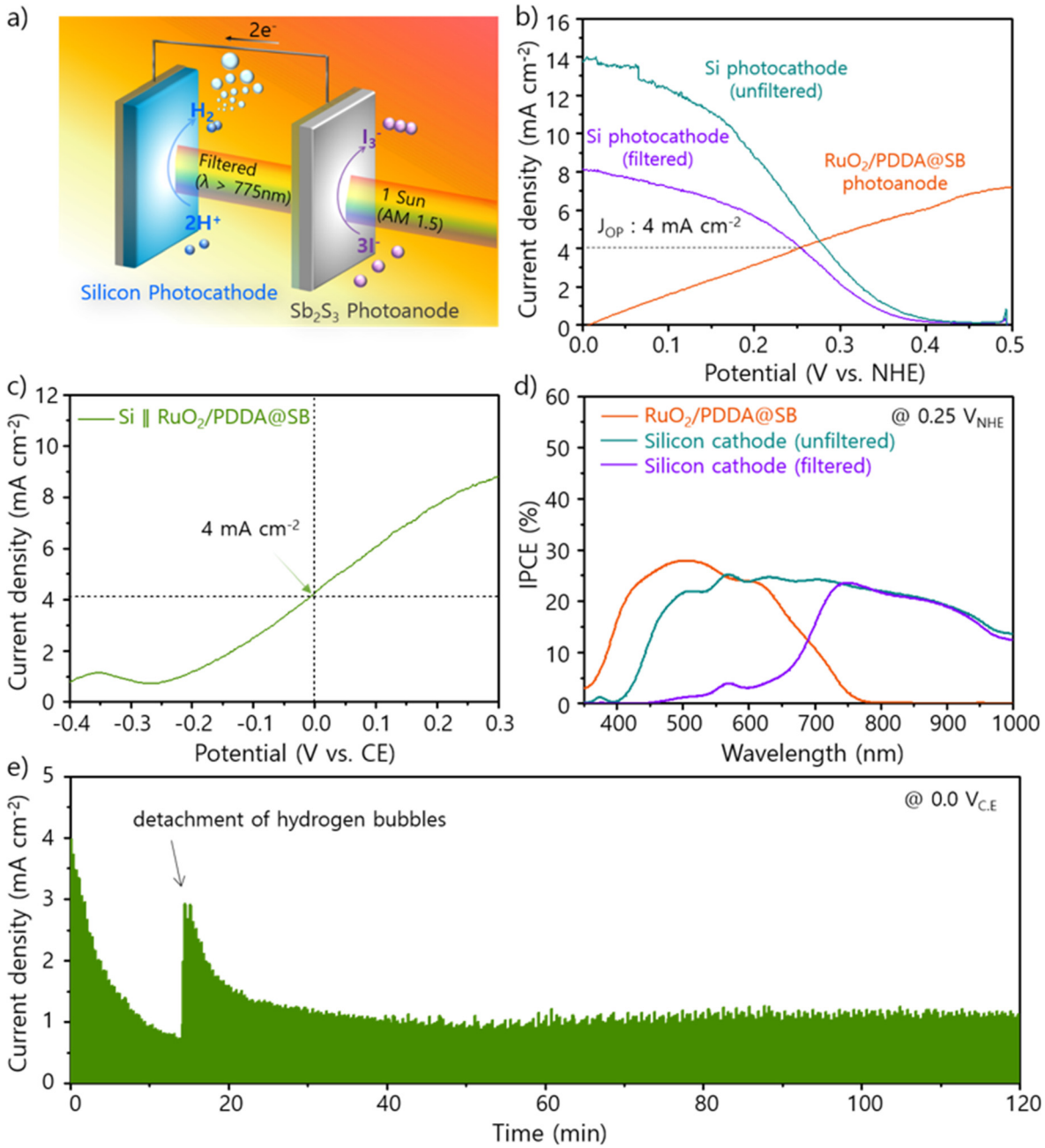

Fig. 5 (a) Schematic of a tandem device comprising a photoanode (RuO_2/PDDA@SB photoanode) and silicon photocathode operated in hydroiodic acid (~pH 1). (b) LSV curves for the RuO_2/PDDA@SB photoanode and silicon photocathode. The operating point is marked for the tandem device (active area: 0.25 cm^2). (c) The LSV curve of Si‖RuO_2/PDDA@SB two-electrode tandem cell (active area: 0.25 cm^2). (d) IPCE at 0.25 V_{NHE} for the Si‖RuO_2/PDDA@SB tandem device. (e) Operation stability under short-circuit condition for the Si‖RuO_2/PDDA@SB tandem device.

LSV curves for RuO_2/PDDA@SB and silicon photocathode in sulfuric acid was formed below 0.4 V_{NHE}, which is the region with no photocurrent spike (Fig. S14, ESI†).

To characterize the photon absorption and utilization capabilities of the HER–IOR tandem configuration of Si‖RuO_2/PDDA@SB, IPCE values of both photoelectrodes were measured at the operating potential (0.25 V_{NHE}). A broad wavelength range of photons could be efficiently exploited by the dual absorbers of Sb_2S_3 (up to 775 nm) and Si (500–1000 nm), as illustrated in Fig. 5(d). The maximum IPCE value of the RuO_2/PDDA@SB photoanode was ~30%, whereas that of the Si photocathode was ~20% and ~25% behind and without RuO_2/PDDA@SB front photoanode, respectively. The photocurrent density estimated by integrating the IPCE results for both the two photoelectrodes reached nearly 4 mA cm^{-2}, which well matches with the determined photocurrent density of the operation point in Fig. 5(b). Moreover, the average H_2 generation faradaic efficiency was 71% according to the gas chromatography

Published on 30 September 2022. Downloaded by Yonsei University on 11/10/2022 12:23:28 AM.

analysis (Fig. S15, ESI†). The additionally occurring reduction of triiodide to iodide (*i.e.*, $I_3^- + 2e^- \rightarrow 3I^-$) at the photocathode likely caused this efficiency deviation. This is because the conduction band of silicon is more negative than HER potential as well as redox level of iodide/triiodide,[7] inducing the silicon photocathode to be capable of reducing not only proton but also triiodide (Fig. S16, ESI†). Moreover, it is known that platinum decorated on silicon photocathode as HER catalyst has also superior triiodide reduction capability,[17] simultaneously promoting HER and triiodide reduction over Pt-modified silicon photocathode. Therefore, to improve the faradaic efficiency, the membrane that physically separates anodic and cathodic electrodes will be essential in real solar-driven HER system based on IOR.[7,51] Furthermore, an additional flowing system could prevent this photoelectrolysis system from photocurrent degradation derived from iodide exhaustion as well as increase in pH during overall reaction expressed as eqn (2). The effect of membrane and flowing system was similarly demonstrated in previous reports on AOR, such as glucose oxidation reaction, glycerol oxidation reaction.[52,53] The photocurrent density *versus* time course plot for the PEC tandem Si‖RuO_2/PDDA@SB device at zero bias is displayed in Fig. 5(e). The initial photocurrent density value of 4 mA cm^{-2} decreased to the nearly saturated photocurrent density of 1.2 mA cm^{-2} within 2 h. The photocurrent spike (~15 min) was attributed to the current decrease due to temporally grown hydrogen bubble blocking the device surface (Fig. S17, ESI†), followed by an instant current increase accompanying the bubble detachment.[54] The overall degradation of the photocurrent density may stem from the decreased active sites during the prolonged photoelectrolysis and/or the dissolution of the Sb_2S_3 absorber by the electrolyte penetration through the pinholes of RuO_2/PDDA@SB (Fig. S18, ESI†). Notably, the color of the hydroiodic acid electrolyte changed from transparent yellow to dark red within 2 h, indicating that the iodide oxidation obviously occurred at the photoanode (Fig. S19a, ESI†).[51,55] When the electrolyte was exposed to only illumination without any electrochemical reactions, however, the color of electrolyte was slowly converted from yellow to orange after two weeks and to red after two months, implying sluggish kinetics of spontaneous oxidation of hydroiodic acid (Fig. S19b, ESI†). This spontaneous reaction could be suppressed by removing oxygen in electrolyte; for example, by purging Ar or N_2 gas. For better long-term stability of the HER–IOR tandem device, future research needs to focus on the conformal deposition of the RuO_2/PDDA catalyst on the Sb_2S_3 surface by controlling the wettability between Sb_2S_3 and the colloidal solution of RuO_2/PDDA. Our findings clearly demonstrate the promising potential of the catalyst-modified Sb_2S_3 photoanode when combined with IOR as an AOR for efficient practical unbiased PEC solar-to-hydrogen generation.

Conclusions

Herein, we developed a high-performance PEC tandem device that is capable of driving bias-free HER on a Si photocathode paired and IOR on a Sb_2S_3-based photoanode. Based on the understanding of the molecular interaction between Sb and S depending on the precursor stoichiometry, a closely packed small cuboid-like Sb_2S_3 film with sharp facets was fabricated. The obtained Sb_2S_3 absorber without catalyst layer exhibited an iodide oxidation current density of 6 mA cm^{-2} at 0.54 V_{NHE} with an onset potential of 0.12 V_{NHE}. Then, the RuO_2/PDDA multilayered catalyst was layer-by-layer deposited onto the Sb_2S_3 absorber to increase the IOR catalytic activity. This modification negatively shifted the onset potential to 0 V_{NHE} and improved the photocurrent density up to 10 mA cm^{-2} at 0.54 V_{NHE}. XANES analysis and EXAFS fitting analysis clearly elucidated the roles of the RuO_2/PDDA catalyst: iodide oxidation was enhanced by the catalytic activity and the passivation of Sb_2S_3 surface states. By combining the catalyst-modified Sb_2S_3 photoanode with a silicon photocathode, unassisted PEC hydrogen production was successfully achieved with a high photocurrent density of 4 mA cm^{-2}. Our results demonstrate the promising prospect of RuO_2-modified Sb_2S_3 photoanode when coupled with IOR for unbiased PEC hydrogen generation.

Experimental section

Preparation of precursor inks

For the Sb_2S_3 absorber inks, 0.254, 0.381, or 0.507 g of $SC(NH_2)_2$ (Sigma-Aldrich, 98%, USA), corresponding to thiourea/$SbCl_3$ stoichiometric ratios of 0.5, 1, 2, respectively, was dissolved in 5 mL of 2ME (Sigma-Aldrich, ≥99.0%, USA). Then, 1.52, 1.14, or 0.760 g of $SbCl_3$ (99.99%, Alfa Aesar, Heysham, UK) was dissolved in the above solution. The resulting inks were stirred at 25 °C for 2 h in a glove box with N_2 atmosphere.

Fabrication of the Sb_2S_3 absorber

The TiO_2 layer was prepared according to a previous study.[56] Three different precursor inks were spin-coated onto TiO_2/FTO/glass substrate at 2500 rpm for 25 s. Before the spin-coating, the prepared substrates were irradiated with UV light for 15 min. After the spin-coating, the as-coated substrates were dried on a hotplate at 180 °C for 3 min and at 300 °C for 3 min in a N_2-filled glove box. Spin-coating was performed five times and the resulting films were annealed at 350 °C for 20 min in a N_2-filled glove box.

Deposition of the RuO_2/PDDA catalyst layer

The colloidal solution of RuO_2 NS was obtained by exfoliating protonated $Na_{0.2}RuO_2$ with tetrabutylammonium (TBA^+) ions for 10 days as previously reported.[57] The RuO_2/PDDA@SB photoanode was prepared as follows: prior to the RuO_2 NS deposition, the Sb_2S_3 absorber was pre-coated with polycations by immersing it in an aqueous PDDA solution (2 mg ml^{-1}) with pH 9 (pH was controlled by TBA·OH addition) for 20 min, yielding a positively charged surface state. After gently rinsing with distilled water, the PDDA-coated Sb_2S_3 absorber was dipped into the colloidal suspension of negatively charged RuO_2 NS (0.08 mg mL^{-1}) with pH 9 (pH was controlled by HCl addition) for 20 min and then cleaned with distilled water

 This journal is © The Royal Society of Chemistry 2022

Published on 30 September 2022. Downloaded by Yonsei University on 11/10/2022 12:23:28 AM.

(inset of Fig. S17, ESI†). After this process was repeated a few times, the prepared RuO_2/PDDA@SB photoanode was dried at 40 °C.

Fabrication of the silicon photocathode

A single-crystal wafer of p-type silicon (boron-doped) was prepared with a size of 4 × 4 cm^2. For cleaning, the wafer was sonicated in acetone, deionized water, and ethanol for 15 min each. The native SiO_2 layer was etched by dipping into hydrofluoric acid for 15 min and then the polyelectrolyte layer was deposited. Subsequently, the n-type TiO_2 layer was deposited onto the modified silicon surface *via* atomic layer deposition. Titanium(IV) tetrakis(dimethylamido) (Easychem, Korea) and H_2O were employed as titanium and oxygen sources, respectively. The deposition process was performed for 920 cycles at 120 °C. A platinum catalyst was deposited on the TiO_2-modified silicon photoelectrode using a 108 Auto Sputter Coater (Ted Pella, Redding, CA, USA).

Characterizations

The liquid Raman spectra (LabRam Aramis, Horiba, Japan) of three different precursor inks were obtained using an Ar-ion laser beam with a 514.5 nm radiation wavelength. The microstructures of the Sb_2S_3 absorbers were identified using a field-emission SEM (Jeol, JSM-IT-500HR, Japan). The Sb/S ratio of the absorber layer was characterized *via* EDX at an acceleration voltage of 15 kV. The crystal structure of the 0.5TU–Sb-ink-based Sb_2S_3 absorber was evaluated *via* XRD (MiniFlex 600, Rigaku, Tokyo, Japan) with Cu K_α radiation (λ = 0.15406 nm). Raman analysis of the 0.5TU–Sb-ink-based Sb_2S_3 absorber was performed using a LabRam Aramis spectrometer (Horiba, Japan) equipped with a charge-coupled device camera. The excitation source was the 532 nm line of an Ar-ion laser with a beam intensity of 1.0 mW. The optical absorbance spectra were obtained using a UV-vis spectrophotometer (V-670, JASCO, Easton, MD, USA) equipped with an integrating sphere. The Tauc plot was obtained to investigate the optical band gap of the 0.5TU–Sb-ink-based Sb_2S_3 absorber according to the absorbance results. For the structural analysis and EDX elemental mapping of the RuO_2/PDDA@SB photoanode, TEM (Jeol, JEM-ARM200F, Japan) was performed at 200 kV acceleration voltage. The focused ion beam lift-out process was conducted for the sample preparation. Noncontact mode KPFM (NX-10, Park systems) was performed two times at ambient atmosphere using a gold-coated silicon cantilever to obtain the topography and corresponding surface potentials for both SB and RuO_2/PDDA@SB photoanodes under dark and light intensity of 30 mW cm^{-2} using portable light source (66088-LED, Newport Corporation, USA). The surface chemical information of the SB and RuO_2/PDDA@SB photoanodes was analyzed *via* XPS (K-alpha, Thermo Scientific Inc., UK). All XPS spectra were calibrated based on the C 1s peak (binding energy of 284.6 eV). Sb K-edge and Ru K-edge XANES/EXAFS analyses were conducted at beam line 10C of the Pohang Accelerator Laboratory (PAL, Pohang, Korea). The energy calibration for the collected XANES/EXAFS spectra was performed by simultaneously measuring the reference spectra of Ru and Sb_2O_5. All the XANES/EXAFS measurements were performed at room temperature in fluorescence mode using gas-ionization detectors. The negative zeta potential of RuO_2 NS was verified using a Malvern Zetasizer Nano ZS (Fig. S20, ESI†).

Photoelectrochemical measurements

PEC measurements were performed using a potentiostat (SI 1287, Solartron, UK) in hydroiodic acid with a three-electrode configuration (Pt coil and Ag/AgCl/KCl (4 M) as the counter and reference electrodes, respectively). A commercial AM 1.5G solar simulator and a Si reference cell (Newport Corporation, USA) were utilized for the simulated sunlight and 1 sun calibration, respectively. For all the PEC measurements, the applied potentials were based on the NHE scale for comparison with other studies. The potential was converted as follows:

$$E_{NHE} = E_{Ag/AgCl} + 0.197 \quad (3)$$

EIS was performed in the frequency of range of 100 kHz–0.1 Hz under 1 sun irradiation at 0.35 V_{NHE} with an alternating current amplitude of 10 mV. Additionally, IPCE and IMVS measurements were performed using an electrochemical workstation (Zennium, Zahner, Germany) and a potentiostat (PP211, Zahner, Germany) with a monochromatic light source (TLS03, Zahner). IMVS measurements were performed in an open-circuit condition with a light intensity of 30 mW cm^{-2}. Mott–Schottky (MS) measurements were performed at a frequency of 10 kHz. The flat band potential (V_{FB}) and charge carrier density (N_A) were obtained by relating C^{-2} against the applied potential as follows:

$$C^{-2} = (2/\varepsilon\varepsilon_0 A^2 e N_A)[V - V_{FB} - (k_B T)/e] \quad (4)$$

Gas chromatography (6500GC system, YL instrument, Anyang, Korea) was performed using a pulsed discharge detector and a molecular sieve column to analyze the H_2 evolution. All the device connections were completely sealed with rubber bulkheads to prevent gas leakage from the quartz reactor.

Conflicts of interest

There are no conflicts to declare.

Acknowledgements

This research was supported by the National R&D Program through the National Research Foundation of Korea (NRF), funded by the Ministry of Science and ICT (2020R1A2C 3008671, 2021R1A3B1068920, and 2021M3H4A1A03049662). This research was also supported by the Yonsei Signature Research Cluster program of 2021 (2021-22-0002). The experiments at PAL were supported in part by MOST and POSTECH.

References

1 T. Tran-Phu, Z. Fusco, I. Di Bernardo, J. Lipton-Duffin, C. Y. Toe, R. Daiyan, T. Gengenbach, C. H. Lin, R. H. Bo,

Published on 30 September 2022. Downloaded by Yonsei University on 11/10/2022 12:23:28 AM.

H. T. Nguyen, G. M. J. Barca, T. Wu, H. J. Chen, R. Amal and A. Tricoli, *Chem. Mater.*, 2021, **33**, 3553.
2 L. F. Pan, J. H. Kim, M. T. Mayer, M.-K. Son, A. Ummadisingu, J. S. Lee, A. Hagfeldt, J. S. Luo and M. Gratzel, *Nat. Catal.*, 2018, **1**, 412.
3 D. W. Huang, L. T. Li, K. Wang, Y. Li, K. Feng and F. Jiang, *Nat. Commun.*, 2021, **12**, 3795.
4 Y.-H. Wu, D. A. Kuznetsov, N. C. Pflug, A. Fedorov and C. R. Muller, *J. Mater. Chem. A*, 2021, **9**, 6252.
5 K. Zhang, M. Ma, P. Li, D. H. Wang and J. H. Park, *Adv. Energy Mater.*, 2016, **6**, 1600602.
6 C. R. Lhermitte and K. Sivula, *ACS Catal.*, 2019, **9**, 2007.
7 L. Yao, Y. P. Liu, H.-H. Cho, M. Xia, A. Sekar, B. P. Darwich, R. A. Wells, J.-H. Yum, D. Ren, M. Gratzel, N. Guijarro and K. Sivula, *Energy Environ. Sci.*, 2021, **14**, 3141.
8 S. Park, W. J. Chang, C. W. Lee, S. Park, H.-Y. Ahn and K. T. Nam, *Nat. Energy*, 2017, **254**, 16185.
9 S. Ardo, S. H. Park, E. L. Warren and N. S. Lewis, *Energy Environ. Sci.*, 2015, **8**, 1484.
10 W. Cui, S. Wu, F. J. Chen, Z. H. Xia, Y. G. Li, X.-H. Zhang, T. Song, S.-T. Lee and B. Q. Sun, *ACS Nano*, 2016, **10**, 9411.
11 G. Seo, B. Kim, S. W. Hwang, S. S. Shin and I. S. Cho, *Nano Energy*, 2021, **80**, 105568.
12 R. Irani, P. Plate, C. Hohn, P. Bogdanoff, M. Wollgarten, K. Hoflich, R. van de Krol and F. F. Abdi, *J. Mater. Chem. A*, 2020, **8**, 5508.
13 P. Subramanyam, M. Deepa, S. S. K. Raavi, H. Misawa, V. Biju and C. Subrahmanyam, *Nanoscale Adv.*, 2020, **2**, 5591.
14 H. Deng, Y. Y. Zeng, M. Ishaq, S. J. Yuan, H. Zhang, X. K. Yang, M. M. Hou, U. Farooq, J. L. Huang, K. W. Sun, R. Webster, H. Wu, Z. H. Chen, F. Yi, H. S. Song, X. J. Hao and J. Tang, *Adv. Funct. Mater.*, 2019, **29**, 1901720.
15 J. A. Christians, D. T. Leighton and P. V. Kamat, *Energy Environ. Sci.*, 2014, **7**, 1148.
16 S. Hu, N. S. Lewis, J. W. Ager, J. H. Yang, J. R. McKone and N. C. Strandwitz, *J. Phys. Chem. C*, 2015, **119**, 24201.
17 I. J. Peter, S. Vijaya, S. Anandan and P. Nithiananthi, *Electrochim. Acta*, 2021, **390**, 138864.
18 S.-J. Sung, E. K. Gil, S.-J. Lee, Y. C. Choi, K.-J. Yang, J.-K. Kang, K. Y. Cho and D.-H. Kim, *J. Ind. Eng. Chem.*, 2017, **56**, 196.
19 W. Yang, J. Ahn, Y. Oh, J. Tan, H. Lee, J. Park, H.-C. Kwon, J. Kim, W. Jo, J. Kim and J. Moon, *Adv. Energy Mater.*, 2018, **8**, 1702888.
20 I. I. Ozturk, N. Kourkoumelis, S. K. Hadjikakou, M. J. Manos, A. J. Tasiopoulos, I. S. Butler, J. Balzarini and N. Hadjiliadis, *J. Coord. Chem.*, 2011, **64**, 3859.
21 W. Yang, Y. Oh, J. Kim, M. J. Jeong, J. H. Park and J. Moon, *ACS Energy Lett.*, 2016, **1**, 1127.
22 B. A. Sorenson, L. U. Yoon, E. Holmgren, J. J. Choi and P. Clancy, *J. Mater. Chem. A*, 2021, **9**, 3668.
23 G. Murtaza, M. Akhrar, M. A. Malik, P. O'Brien and N. Revaprasadu, *Mater. Sci. Semicond. Process.*, 2015, **40**, 643.
24 Q. Wang, F. Y. Liu, L. Wang, L. X. Jiang, Q. Y. Wang, B. Hong and Y. Q. Lai, *Scr. Mater.*, 2019, **173**, 75.
25 N. Singhal, R. Chakraborty, P. Ghosh and A. Nag, *Chem. – Asian J.*, 2018, **13**, 2085.
26 R. Parize, A. Katerski, I. Gromyko, L. Rapenne, H. Roussel, E. Karber, E. Appert, M. Krunks and V. Consonni, *J. Phys. Chem. C*, 2017, **121**, 9672.
27 N. H. Kwon, J. M. Lee, T.-H. Gu, X. Jin and S.-J. Hwang, *Sol. RRL*, 2021, **5**, 2000411.
28 D. Y. W. Yu, P. V. Prikhodchenko, C. W. Mason, S. K. Batabyal, J. Gun, S. Sladkevich, A. G. Medvedev and O. Lev, *Nat. Commun.*, 2013, **4**, 2922.
29 F. S. Li, H. Yang, Q. M. Zhuo, D. H. Zhou, X. J. Wu, P. L. Zhang, Z. Y. Yao and L. C. Sun, *Angew. Chem., Int. Ed.*, 2021, **60**, 1976.
30 T. G. Vo, C. C. Kao, J. L. Kuo, C. C. Chiu and C. Y. Chiang, *Appl. Catal., B*, 2020, **278**, 119303.
31 Z. L. Tian, P. F. Zhang, P. Qin, D. Sun, S. N. Zhang, X. W. Guo, W. Zhao, D. Y. Zhao and F. Q. Huang, *Adv. Energy Mater.*, 2019, **9**, 1901287.
32 J. J. Suo, B. W. Yang, E. Mosconi, H.-S. Choi, Y. Kim, S. M. Zakeeruddin, F. De Angelis, M. Gratzel, H.-S. Kim and A. Hagfeldt, *Adv. Funct. Mater.*, 2021, **31**, 2102902.
33 X.-D. Wang, Y.-H. Huang, J.-F. Liao, Z.-F. Wei, W.-G. Li, Y.-F. Xu, H.-Y. Chen and D.-B. Kuang, *Nat. Commun.*, 2021, **12**, 1202.
34 P. Wei, W. Y. Zhao, D. G. Tang, W. T. Zhu, X. L. Nie and Q. J. Zhang, *J. Materiomics*, 2016, **2**, 280.
35 L. Chen, X. L. Chen, F. Y. Liu, H. H. Chen, H. Wang, E. L. Zhao, Y. Jiang, T.-S. Chan, C.-H. Wang, W. H. Zhang, Y. Wang and S. F. Chen, *Sci. Rep.*, 2015, **5**, 11514.
36 Z. Y. Wu, N. L. Saini, S. Agrestini, D. Di Castro, A. Bianconi, A. Marcelli, M. Battisti, D. Gozzi and G. Balducci, *J. Phys.: Condens. Matter*, 2000, **12**, 6971.
37 T.-H. Gu, D. A. Agyeman, S. J. Shin, X. Jin, J. M. Lee, H. Kim, Y.-M. Kang and S.-J. Hwang, *Angew. Chem., Int. Ed.*, 2018, **57**, 15984.
38 A. Kyono, A. Hayakawa and M. Horiki, *Phys. Chem. Miner.*, 2015, **42**, 475.
39 S.-J. Hwang, H.-S. Park, J.-H. Choy and G. Campet, *Chem. Mater.*, 2000, **12**, 1818.
40 S. H. Wang, Y. Cheng, H. J. Xue, W. Q. Liu, Z. Yi, L. M. Chang and L. M. Wang, *J. Mater. Chem. A*, 2021, **9**, 7838.
41 Q. Xiao, C.-X. Hu, H.-R. Wu, Y.-Y. Ren, X.-Y. Li, Q.-Q. Yang, G.-H. Dun, Z.-P. Huang, Y. Peng, F. Yan, Q. Wang and H.-L. Zhang, *Nanoscale Horiz.*, 2020, **5**, 124.
42 C. P. Thao, T. T. A. Tuan, D.-H. Kuo, W.-C. Ke and T. T. V. S. Na, *Coatings*, 2020, **10**, 210.
43 W. Wang, S. R. Guo, I. Lee, K. Ahmed, J. B. Zhong, Z. Favors, F. Zaera, M. Ozkan and C. S. Ozkan, *Sci. Rep.*, 2014, **4**, 4452.
44 J. Han, S. J. Wang, J. B. Yang, S. H. Guo, Q. Cao, H. J. Tang, X. Y. Pu, B. Y. Gao and X. H. Li, *ACS Appl. Mater. Interfaces*, 2020, **12**, 4970.
45 K. Krishnamoorthy, P. Pazhamalai and S. J. Kim, *Electrochim. Acta*, 2017, **227**, 85.
46 S. Kubendhiran, R. Sakthivel, S.-M. Chen, R. Anbazhagan and H.-C. Tsai, *Composites, Part B*, 2019, **168**, 282.
47 H. Ezzouia, R. Heindl, R. Parsons and H. Tributsch, *J. Electroanal. Chem. Interfacial Electrochem.*, 1984, **165**, 155.
48 C. Ding, J. Shi, Z. Wang and C. Li, *ACS Catal.*, 2017, **7**, 675–678.

 This journal is © The Royal Society of Chemistry 2022

Published on 30 September 2022. Downloaded by Yonsei University on 11/10/2022 12:23:28 AM.

49 H. Wang, Y. Xia, H. Li, X. Wang, Y. Yu, X. Jiao and D. Chen, *Nat. Commun.*, 2020, **11**, 3078.
50 J. Segura-Salazar and P. R. Brito-Parada, *Miner. Eng.*, 2021, **15**, 106713.
51 D. B. Adam, M.-C. Tsai, Y. A. Awoke, W.-H. Huang, Y.-W. Yang, C.-W. Pao, W.-N. Su and B. J. Hwang, *ACS Sustainable Chem. Eng.*, 2021, **9**, 8803.
52 Y. Zhang, B. Zhou, Z. Wei, W. Zhou, D. Wang, J. Tian, T. Wang, S. Zhao, J. Liu, L. Tao and S. Wang, *Adv. Mater.*, 2021, **33**, 2104791.
53 L. Fan, Y. Ji, G. Wang, J. Chen, K. Chen, X. Liu and Z. Wen, *J. Am. Chem. Soc.*, 2022, **144**, 7224–7235.
54 H. Lin, S. Li, G. Yang, K. Zhang, D. Tang, Y. Su, Y. Li, S. Luo, K. Chang and J. Ye, *Adv. Funct. Mater.*, 2021, **31**, 2007071.
55 T. Yang, H. Wang, X.-M. Ou, C.-S. Lee and X.-H. Zhang, *Adv. Mater.*, 2012, **24**, 6199.
56 S.-C. Yun, S. Ma, H.-C. Kwon, K. Kim, G. Jang, H. Yang and J. Moon, *Nano Energy*, 2019, **59**, 481.
57 K. Fukuda, T. Saida, J. Sato, M. Yonezawa, Y. Takasu and W. Sugimoto, *Inorg. Chem.*, 2010, **49**, 4391.